Quasi-Static Crush Modelling of Carbon/Epoxy Composites with Discontinuous Galerkin/Anisotropic Extrinsic Cohesive Law Method

Xing Liu [1,2,*], Ling Wu [1,3], Danny Van Hemelrijck [1], and Lincy Pyl [1]

[1] Department of Mechanics of Materials and Constructions, Vrije Universiteit Brussel (VUB), Pleinlaan 2, B-1050 Brussels, Belgium

[2] SIM M3 Program, Technologiepark 48, BE-9052 Zwijnaarde, Belgium

[3] Department of Aeronautics and Astronautics, Computational & Multiscale Mechanics of Materials, University of Liège, Allée de la découverte 9, B-4000 Liège, Belgium

Abstract

Carbon/epoxy composites demonstrate significant promising improvements of weight to performance in the automotive industry. However, the design of carbon/epoxy composite components for crashworthiness remains challenging and normally requires laborious and repeated experimental work. This study adopts a predictive crush model of carbon/epoxy composites, which can partially replace the experimental work. The discontinuous Galerkin (DG) method with extrinsic cohesive laws is employed to simulate the failure patterns in the composite structures. The application of DG distinguishes the fracture model from the conventional approach where preset cohesive elements are used on the location where cracks are expected. The mixed mode cohesive laws are used to simulate the delamination between each layer. To capture different crack propagations in different layups, the anisotropic cohesive law is used to simulate the intralaminar crack propagation in composites. To verify the adopted model, circular composite tube specimens with different layups have been simulated and compared with tests under quasi-static crush loadings. The comparisons of numerical results with experimental data show that the DG crush model can reproduce the experimental results with relatively high accuracy.

Keywords: crush modelling, carbon/epoxy, Discontinuous Galerkin method, mixed mode delamination, anisotropic cohesive law, energy absorption

[*]Corresponding author E-mail address: xing.liu@vub.be

1. Introduction

Composites are highly appreciated for industrial applications where high strength-to-weight and stiffness-to-weight ratios are required, such as the vehicle industry. In these applications, compared with the conventional metallic materials such as aluminium, steel and so on, composites provide better opportunities to improve fuel economy and structural safety [1~3]. The advantages of composite materials on specific energy absorption, strength and stiffness lead to the increased use of them, which further requires the development of the knowledge of the behaviour of composites. This paper focuses on using an advanced numerical tool to investigate the energy absorption behaviour of composite tubes under axial quasi-static crush loadings.

The main goal of designing a crashworthy structure is to limit the passengers' injury by making the structure to absorb most crush energy and reduce the peak crush load [4][5]. To study the energy absorption behaviour and carry out the failure analysis of composites by experiments can be rather money and time consuming, especially when various loading conditions are required. Therefore, the numerical analyses, which are also called virtual experiments, are rapidly developed. Many experimental studies on composites [6~9] have proved that the peak load is controlled by the start of circumferential delamination, so the numerical approach reproducing the delamination failure is important to predict the correct energy absorption. In the crushing model of Pinho [10], the delamination was reproduced by the cohesive zone method (CZM) and initiated by a triangular rigid wedge. However, in this work only a single petal of the crushed tube was modelled, which means before the simulation the number of crushed petals should be known, and all petals should share the same size and shape. The work of Pinho proves the promising application of cohesive methods in reproducing the delamination between composite laminates. Because composite laminates are commonly modelled by shell elements, the stacked shell model was approached by joining layers together using cohesive elements to simulate the crush process. In this way, the model is also more realistic to the true structures than the single layer model. A stacked shell model of a corrugated carbon fibre reinforced plastic (CFRP) plate was presented by Sololinsky et al [11], which shows a good quantitative and qualitative agreement with experimental data and exhibits robustness with respect to the input material properties in quasi-static loading cases. Xiao et.al. [12] also adopted the stacked shell model and applied the composite damage constitutive laws (MAT 58 in LS-DYNA) for dynamic axial crush simulation of braided carbon tubes.

In the above models, the intralaminar failure was considered in the ply damage models, which use a modulus evolution or reduction. The combination of using the cohesive elements for delamination (interlaminar failure) and using continuum damage models for ply damage (intralaminar failure) [13][14], asking the use of two different kinematic representations for interlaminar and intralaminar failures, presents some fundamental problems. For example, as mentioned in Ref. [15], when modelling the interaction between transverse matrix cracks and delamination, the high stress at the tip of the transverse crack needs to be captured. However, with this combination method, this interaction cannot be captured, because the elements where the transverse crack is predicted soften without being able to accurately capture the stress field at the interface. To simulate the axial crack propagations in the composite layers, Palanivelu et al. [16] adopted pre-set seam elements in the stacked shell model. As the crack propagation position was predefined, this leads to a model which is not fully predictive.

The intrinsic cohesive law has proved to be an efficient and accurate tool to simulate crack initiation and propagation at a priori defined interfaces, also the intrinsic cohesive laws were used to simulate the interactions between intralaminar and interlaminar failure mechanisms through inserting cohesive elements between all bulk elements [17][18]. However, researchers have shown that such a scheme not only exhibits a strong mesh dependency but also alters the structural stiffness [19]. The intrinsic cohesive law does not satisfy the consistency condition due to the initial slope in the reversible part (the ascending slope in Fig.1 a) of the cohesive law, adding spurious stiffness elements in a mesh dependent way, which softens the structure. Although this error can be reduced by increasing the initial slope [20][21], this leads to an ill conditioned stiffness matrix for static simulations or to unacceptable small values of the critical time step for explicit dynamic simulations [22].

The drawbacks inherent to the intrinsic cohesive law can be avoided by using an extrinsic cohesive law [23][24], which models only the irreversible part of the response as shown in Fig.1 b). Practically the simulation proceeds with a classical finite element approach and cohesive elements are introduced at the interface of elements at the onset of fracture. Based on the method used in the 2D cohesive-law fracture model in [23], Lee et.al. [25] implemented the node separation method with cohesive law for the tensile failure and Mohr-Coulomb model for the compressive loading in a 3D model, and verified this model in an oblique impact test on a three layer composite system. Besides, instead of using a cohesive law, Zhang et.al. [26] combined the

anisotropic behaviour of composite laminate with the nonlinear equation of state behaviour, and implemented it in an orthotropic node-separation finite element method model to represent the hypervelocity impact behaviour/damage of composite laminates. This model was verified by corresponding experimental data and proved to be capable to capture the damage behaviour of composite laminates in the hypervelocity impact case. However, the 3D implementation of this framework is not straightforward because the mesh topology changes during the computation. To implement CZM in a 3D fracture model to predict the intralaminar failure, two methods are presented. One is the extended finite element method (XFEM) combined with CZM [27][28]. With XFEM the entire crack propagation paths are independent of the meshes, so the predefined meshes are not necessary. Vigueras et al. [15] proposed a coupled XFEM/CZM method, which can perfectly capture both interlaminar and intralaminar failures for the open hole tensile test of a quasi-isotropic laminate sequence. The other method is a hybrid discontinuous Galerkin/cohesive zone model (DG/CZM) [29~33]. This method allows an extrinsic cohesive law to be integrated on the already existing interface elements once a fracture criterion is met, without requiring mesh topology changes. In this work, to capture the intralaminar failure patterns, the discontinuous Galerkin (DG) method with extrinsic cohesive laws (ECL) is adopted.

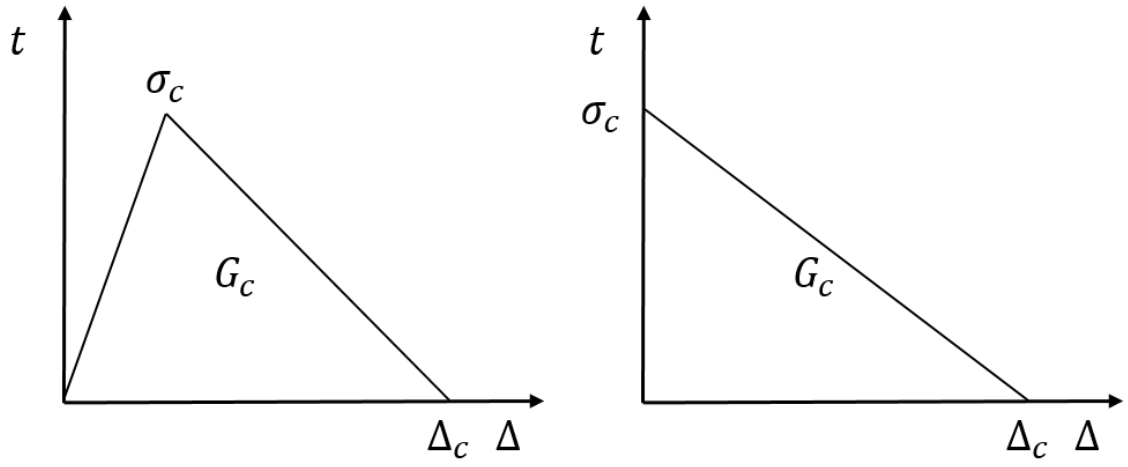

a) Intrinsic cohesive law b) Extrinsic cohesive law

Fig.1 Cohesive law

In this work, to capture the different possible crack propagations in each layer, based on the DG model, the anisotropic cohesive law is used. Besides, in the explicit solver, to accelerate the computation process in static/quasi-static cases, higher loading velocity instead of the physical one is commonly used. The loading velocity in the simulation is chosen to avoid local response (stress

concentration due to the high speed loading) and motivate the global response (stress wave can propagate through the whole structure and be balanced in the loading process). Therefore, to investigate the effects of different loading velocities on this model and find a suitable loading velocity in this simulation case, various loading velocities (10 m/s, 20m/s, and 30m/s) have been investigated.

The presented DG/anisotropic cohesive law model in our paper adopts explicit solver, so it can be easily applied to the dynamic problem [30][33]. With really fine mesh, there is no difference between the static simulation and dynamic simulation. In fact, because the computation time step in the explicit solver is identified by the material properties and mesh sizes, instead of the loading speed, from this aspect, the static problem is more challenging than the dynamic one because of its much longer simulation time.

2. Crush Modelling

2.1 Discontinous Galerkin cohesive zone modelling

The scalable hybrid DG/CZM approach [30~33] can simulate the crack propagations without predefined crack positions. In this method, interface elements are inserted at interelement boundaries at the beginning of the simulation by using a DG approach. Additional terms in the weak formula of the problem are used to guarantee the consistency and stability of the finite element solution in the DG domain. When the stress at an interelement boundary meets the specified fracture criterion, the computation of the DG interface flux terms is replaced by an extrinsic cohesive law. This ECL describes the irreversible traction-separation response on the open interface. The main ideas of the formulation are recalled and summarized below

Let us assume a body Ω subjected to a force per unit mass $\mathbf{B}$. Its boundary surface Γ is separated into two parts: the Dirichlet boundary Γ_D constrained by displacements $\boldsymbol{\varphi}$, and the Neumann boundary Γ_N constrained by a surface traction $\boldsymbol{T}$. Then the continuum equations stated in the material form are:

$$\rho_0 \ddot{\boldsymbol{u}} = \nabla_0 \cdot \mathbf{P}^T + \rho_0 \mathbf{B} \text{ in } \Omega \quad \text{Eq. 1}$$

$$\boldsymbol{u} = \boldsymbol{\varphi} \text{ on } \Gamma_D \quad \text{Eq. 2}$$

$$\mathbf{P} \cdot \boldsymbol{N} = \boldsymbol{T} \text{ on } \Gamma_N \quad \text{Eq. 3}$$

In the above equations, $\boldsymbol{u}$ is the displacement, ρ_0 is the initial density, $\mathbf{P}$ is the first Piola-Kirchhoff stress tensor, $\boldsymbol{N}$ is the outward unit surface normal in the reference configuration. The

finite element discretization of the body Ω is expressed as $\Omega = \cup\, \Omega_e$, where $\cup\, \Omega_e$ is the union of the open domain Ω_e with its boundary Γ_e.

The DG weak form of Eq. 1~3 is obtained by seeking a polynomial approximation $\boldsymbol{u}$ of the deformation over the discretization Ω. For a DG formulation, the test functions $\boldsymbol{w}$ are discontinuous across the element interfaces on the internal boundary of the body $\Gamma_i = \cup\, \Gamma_e \backslash \Gamma$. The strong form Eq. 1 of the linear momentum balance is enforced in a weighted-average sense by multiplying it with the test function $\boldsymbol{w}$ and integrating by parts in the domain. However, because the test function is discontinuous, the integration by parts is only performed on each element, which leads to the weak form:

$$\sum_e \int_{\Omega_e} (\rho_0 \ddot{\boldsymbol{u}} \cdot \boldsymbol{w} + \boldsymbol{P} : \nabla_0 \boldsymbol{w}) dV - \sum_e \int_{\Gamma_e \cap \Gamma_i} \boldsymbol{w} \cdot \boldsymbol{P} \cdot \boldsymbol{N} dS = \sum_e \int_{\Omega_e} \rho_0 \boldsymbol{B} \cdot \boldsymbol{w} dV + \sum_e \int_{\Gamma_e \cap \Gamma_N} \boldsymbol{w} \cdot \mathbf{T} dS \quad \text{Eq. 4}$$

Considering the discretization $\Omega = \cup\, \Omega_e$, the Eq. 4 can be written as:

$$\int_\Omega (\rho_0 \ddot{\boldsymbol{u}} \cdot \boldsymbol{w} + \mathbf{P} : \nabla_0 \boldsymbol{w}) dV + \int_{\Gamma_i} [\![\boldsymbol{w} \cdot \mathbf{P}]\!] \cdot \boldsymbol{N}^- dS = \int_\Omega \rho_0 \mathbf{B} \cdot \boldsymbol{w} dV + \int_{\Gamma_N} \boldsymbol{w} \cdot \mathbf{T} dS \quad \text{Eq. 5}$$

In this equation, the discretized stress tensor **P** results from the discretized deformation gradient state $\mathbf{F} = \nabla \mathbf{u} + \mathbf{I}$ through a constitutive material law (as detailed in Appendix). Here a jump operator and an average operator are separately defined by:

$$[\![\cdot]\!] = [\cdot^+ - \cdot^-] \text{ and } \langle \cdot \rangle = \frac{1}{2} [\cdot^+ + \cdot^-]$$

The two operators are defined on an interface of two elements, arbitrarily denoted "plus" and "minus" elements. $\boldsymbol{N}^-$ is the outward unit surface normal of the minus element. To address the contribution of the inter-element discontinuity terms by the limit values on the surface from the neighbouring elements (more details in [30]), the second term of Eq. 5 can be written as:

$$\int_{\Gamma_i} [\![\boldsymbol{w} \cdot \mathbf{P}]\!] \cdot \boldsymbol{N}^- dS = \int_{\Gamma_i} [\![\boldsymbol{w}]\!] \cdot \langle \mathbf{P} \rangle \cdot \boldsymbol{N}^- dS + \int_{\Gamma_i} \langle \boldsymbol{w} \rangle \cdot [\![\mathbf{P}]\!] \cdot \boldsymbol{N}^- dS \quad \text{Eq. 6}$$

The last term in Eq. 6 can be omitted while preserving consistency since for the exact solution the stress is continuous. Considering this assumption (more details about the DG considerations can be found in [34]), the weak form Eq. 5 can be simplified to:

$$\int_\Omega (\rho_0 \ddot{\boldsymbol{u}} \cdot \boldsymbol{w} + \mathbf{P} : \nabla_0 \boldsymbol{w}) dV + \int_{\Gamma_i} [\![\boldsymbol{w}]\!] \cdot \langle \mathbf{P} \rangle \cdot \boldsymbol{N}^- dS = \int_\Omega \rho_0 \mathbf{B} \cdot \boldsymbol{w} dV + \int_{\Gamma_N} \boldsymbol{w} \cdot \mathbf{T} dS \quad \text{Eq. 7}$$

Because the inter-element displacement continuity is not enforced in this DG formulation (Eq. 7) and to ensure the stability of the numerical solution, it should be enforced weakly. The compatibility equation $\boldsymbol{u}^+ - \boldsymbol{u}^- = 0$ on Γ_i is enforced through a (sufficiently large)

symmetrisation quadratic stabilization term in $[\![\boldsymbol{u}]\!]$ and $[\![\boldsymbol{w}]\!]$. With the quadratic terms, the general displacement jumps can be stabilized in the numerical solution, and the symmetrisation term can lead to an optimal convergence rate with respect to the mesh size. Then the final weak formulation of the large deformation material response consisting of finding $\boldsymbol{u}$ is:

$$\int_{\Omega} (\rho_0 \ddot{\boldsymbol{u}} \cdot \boldsymbol{w} + \mathbf{P}: \nabla_0 \boldsymbol{w}) dV + \int_{\Gamma_i} [\![\boldsymbol{w}]\!] \cdot \langle \mathbf{P} \rangle \cdot \boldsymbol{N}^- dS + \int_{\Gamma_i} \left\{ [\![\boldsymbol{w}]\!] \otimes \boldsymbol{N}^- : \langle \frac{\beta_s}{h_s} \mathbb{C} \rangle : [\![\boldsymbol{u}]\!] \otimes \boldsymbol{N}^- \right\} dS +$$

$$\int_{\Gamma_i} \{ [\![\boldsymbol{u}]\!] \cdot \langle \mathbb{C}: \nabla_0 \boldsymbol{w} \rangle \cdot \boldsymbol{N}^- \} dS = \int_{\Omega} \rho_0 \mathbf{B} \cdot \boldsymbol{w} dV + \int_{\Gamma_N} \boldsymbol{w} \cdot \mathbf{T} dS \quad \text{Eq. 8}$$

where h_s is the mesh size and β_s plays the role of a penalty parameter for the stabilisation. Besides, $\mathbb{C} = \frac{\partial \mathbf{P}}{\partial \mathbf{F}}$ is the Lagrangian tangent modulus. In the explicit dynamic time integrations, the stable time step is reduced by a factor of $\sqrt{\beta_s}$ in this DG method compared to the continuous Galerkin formulation [35].

Based on the above DG framework, the dynamic simulation proceeds initially and prior to the nucleation of cracks. The onset of fracture is modelled by the extrinsic CZM approach, following a fracture stress criterion. Upon the nucleation of a crack at an interface element, the DG flux terms stop operating and are replaced with the Traction-Separation Law (TSL) which controls the fracture process. This process does not require any modifications of the mesh, but simply changes the terms evaluated at the interface element integration points. Then, if $\boldsymbol{t}$ is the surface traction on the opened interface Γ_{ic} resulting from the TSL in the reference configuration, Eq. 8 becomes:

$$\int_{\Omega} (\rho_0 \ddot{\boldsymbol{u}} \cdot \boldsymbol{w} + \mathbf{P}: \nabla_0 \boldsymbol{w}) dV + \int_{\Gamma_{ic}} \alpha \boldsymbol{t}([\![\boldsymbol{u}]\!]) \cdot [\![\boldsymbol{w}]\!] ds + \int_{\Gamma_i} (1-\alpha) [\![\boldsymbol{w}]\!] \cdot \langle \mathbf{P} \rangle \cdot \boldsymbol{N}^- dS + \int_{\Gamma_i} (1 -$$

$$\alpha) [\![\boldsymbol{w}]\!] \otimes \boldsymbol{N}^- : \langle \frac{\beta_s}{h_s} \mathbb{C} \rangle : [\![\boldsymbol{u}]\!] \otimes \boldsymbol{N}^- dS + \int_{\Gamma_i} (1-\alpha) [\![\boldsymbol{u}]\!] \cdot \langle \mathbb{C}: \nabla_0 \boldsymbol{w} \rangle \cdot \boldsymbol{N}^- dS = \int_{\Omega} \rho_0 \mathbf{B} \cdot \boldsymbol{w} dV +$$

$$\int_{\Gamma_N} \boldsymbol{w} \cdot \mathbf{T} dS \quad \text{Eq. 9}$$

In the above equation α is a binary operator defined as $\alpha = 0$ before fracture and $\alpha = 1$ after the fracture stress criterion is met. We note that the term related to the surface traction on the opened interface Γ_{ic} is expressed in the current configuration, hence the use of the surface ds.

With the hybrid DG/CZM method, no modification of the mesh is required during the shift procedure from the uncracked to a cracked configuration, and only the constitutive formulations at the interface elements are changed. Besides, contrary to the intrinsic CZM, which is restricted by the critical time step size and/or the artificial compliance, this method satisfies the consistency in the pre-fracture stage.

Based on the homemade DG software of CM3 group [36], the anisotropic constitutive law (reported in Appendix), which fits the large deformation problem, the mixed mode extrinsic cohesive law for the delamination simulation between each layer and the anisotropic extrinsic cohesive law (AECL), which allows the different crack propagation directions in different layups, are used in the DG model to simulate the quasi-static crushing process of the composite tubes.

2.2 Delamination

Cohesive elements [37] are widely used to model the interface delamination. The constitutive behaviour of these elements is based on the amount of energy necessary to create new fracture surfaces. Normally the delamination position can easily be predefined on the interface, so intrinsic cohesive laws with pre-set cohesive elements are used. However, in these cases, the TSL also describes the elastic behaviour prior to the delamination, which would yield the mesh-size effects [38][39]. In the above hybrid DG/CZM method, the behaviour before the delamination is involved in the DG form, so the mesh-size effects can be avoided. Therefore, the extrinsic cohesive law is used in this work to simulate the delamination.

2.2.1 Mixed mode initiation criterion

In the composite delamination situation where more than one mode is involved simultaneously, the delamination can be even initiated before the individual strengths in different modes are met. Therefore, to analyse this situation, the quadratic delamination criterion is used for the delamination onset prediction [40][41]. Therefore, the mixed mode initiation criterion is:

$$\left(\frac{\ll\sigma_{\mathrm{n}}\gg}{\sigma_{\mathrm{IC}}}\right)^2+\left(\frac{\sigma_{\tau}}{\sigma_{\mathrm{IIC}}}\right)^2=1 \qquad \text{Eq. 10}$$

where $\sigma_{\mathrm{n}}=\overline{\boldsymbol{n}}\cdot\boldsymbol{t}$ and $\sigma_{\tau}=\sqrt{\boldsymbol{t}\cdot\boldsymbol{t}-(\sigma_{\mathrm{n}})^2}$ are respectively the normal and tangent components of the apparent surface traction $\boldsymbol{t}$ on the delamination interface. Also $\overline{\boldsymbol{n}}$ is the deformed unit normal outward to the surface. σ_{IC} and σ_{IIC} are respectively the critical stresses of the cohesive model in mode I and II. The operator $\ll*\gg=*$, for $*\geq 0$ and $\ll*\gg=0$ for $*<0$. When σ_{n} and σ_{τ} meet Eq. 10, the delamination is initiated, and the values σ_{n} and σ_{τ} are respectively indicated as the initial critical stresses σ_{n0} and $\sigma_{\tau 0}$ as shown in Fig.2.

2.2.2 Mixed mode propagation

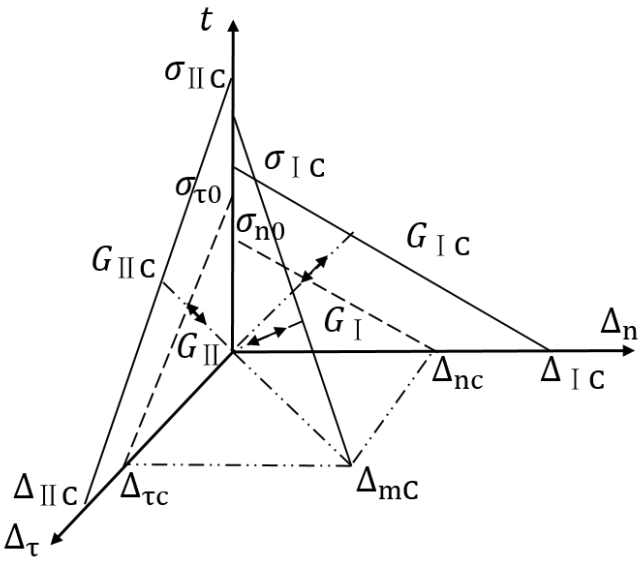

Fig.2 Mixed mode cohesive law for delamination

In the mixed mode delamination situation, the delamination propagation is controlled by the power law criterion [42]:

$$\left(\frac{G_I}{G_{IC}}\right)^{\lambda} + \left(\frac{G_{II}}{G_{IIC}}\right)^{\lambda} = 1 \qquad \text{Eq. 11}$$

where G_{IC} and G_{IIC} are respectively the critical energy release rates in mode I and II. For most carbon/epoxy composites, the mixed mode parameter λ is identified among 1 to 2. In our case, $\lambda = 1$ is used. During the propagation process, G_I and G_{II} are the energy release rates which directly control the process. In the mixed mode opening situation, as shown in Fig.2, with the surface opening vector $\overline{\boldsymbol{u}}$, the effective surface separation Δ^* is identified as:

$$\Delta^* = \sqrt{\ll \Delta_n \gg^2 + (\Delta_\tau)^2} \qquad \text{Eq. 12}$$

where $\Delta_n = \overline{\boldsymbol{u}} \cdot \overline{\boldsymbol{n}}$ and $\Delta_\tau = \overline{\boldsymbol{u}} - \Delta_n \overline{\boldsymbol{n}}$ are respectively the separations along the interface element normal and tangent in its deformed configuration. Then as shown in Fig.2, the critical openings for pure mode I and II and the mixed mode I and II can respectively obtained from $\Delta_{IC} = \frac{2G_{IC}}{\sigma_{IC}}$, $\Delta_{IIC} = \frac{2G_{IIC}}{\sigma_{IIC}}$, $\Delta_{nc} = \frac{2G_I}{\sigma_{n0}}$ and $\Delta_{\tau c} = \frac{2G_{II}}{\sigma_{\tau 0}}$. The participation of the different modes is defined by the parameter $\beta_d = \max\left\{0, \frac{\sigma_\tau}{\sigma_n}\right\}$. Then through Eq. 11 and 12, the critical mixed mode opening Δ_{mC} can be obtained by:

$$\Delta_{\mathrm{mC}}=\begin{cases}\dfrac{2\left(1+\beta_{\mathrm{d}}^{2}\right)}{\sqrt{\ll\sigma_{\mathrm{n0}}\gg^{2}+(\sigma_{\tau 0})^{2}}}\Big/\left[\dfrac{1}{G_{\mathrm{IC}}}+\dfrac{\beta_{\mathrm{d}}^{2}}{G_{\mathrm{IIC}}}\right], & \Delta_{\mathrm{n}}>0\\ \Delta_{\mathrm{II}C} & ,\ \Delta_{\mathrm{n}}\leq 0\end{cases} \quad \text{Eq. 13}$$

Then the mixed mode cohesive law can be expressed as:

$$\sigma_{\mathrm{n}}=\begin{cases}\ll\sigma_{\mathrm{n0}}\gg\left(1-\dfrac{\Delta^{*}}{\Delta_{\mathrm{mC}}}\right), & if\ \dot{\Delta}^{*}\geq 0\ and\ \Delta^{*}=\Delta_{\max}\\ \sigma_{\mathrm{nmax}}\dfrac{\Delta^{*}}{\Delta_{\mathrm{mC}}} & if\ \dot{\Delta}^{*}<0\end{cases} \quad \text{Eq. 14}$$

$$\sigma_{\tau}=\begin{cases}\sigma_{\tau 0}\left(1-\dfrac{\Delta^{*}}{\Delta_{\mathrm{mC}}}\right), & if\ \dot{\Delta}^{*}\geq 0\ and\ \Delta^{*}=\Delta_{\max}\\ \sigma_{\tau\max}\dfrac{\Delta^{*}}{\Delta_{\mathrm{mC}}} & if\ \dot{\Delta}^{*}<0\end{cases} \quad \text{Eq. 15}$$

where $\Delta_{\max}$ is the maximum opening at the current time step, σ_{nmax} and $\sigma_{\tau\max}$ are the normal and tangential components of $\boldsymbol{t}$ when the maximum opening $\Delta_{\max}$ is reached.

2.3 Intralaminar fracture

The traction separation law is given by the cohesive law applied in the DG model. However, in different layups the crack propagates in different directions, which means that the fracture properties of the composites are also anisotropic. Therefore, instead of conventional isotropic cohesive laws, the AECL has been used in this model. The AECL is based on the method of the effective fracture strength calculation presented in the work [43].

2.3.1 Anisotropic cohesive law initiation criterion

Normally, in the isotropic cohesive law, the critical strength σ_{c} is a constant, but in the anisotropic cohesive law, the critical strength should be identified by the direction. In a composite with anisotropic fracture behaviour, the critical strength σ_{c} and critical energy dissipation G_{c} are measured on the planes on which their norms are along the principle directions of the material. Therefore, the fracture properties are the following 6 parameters: $\sigma_{\mathrm{c}}^{1}, G_{\mathrm{c}}^{1}, \sigma_{\mathrm{c}}^{2}, G_{\mathrm{c}}^{2}, \sigma_{\mathrm{c}}^{3}, G_{\mathrm{c}}^{3}$.

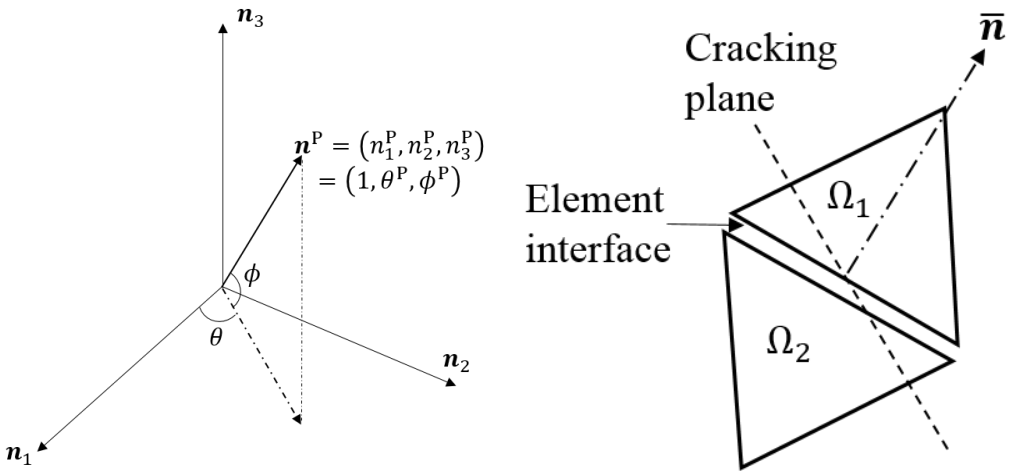

a) b)

Fig.3 Coordinates and planes in the anisotropic cohesive law

Direction 3 is the longitudinal direction (fibre orientation) of the composite laminate;

Direction 1 and 2 are the transverse directions of the composite laminate.

Considering another plane whose normal is not in the principle directions, the normal can be expressed in the material coordinate system with three orthogonal directions which correspond to the principle directions of anisotropic materials $(\boldsymbol{n}_1, \boldsymbol{n}_2, \boldsymbol{n}_3)$. Here we assume that the material system is orthonormal, and remains so in the deformed configuration, which is justified because of the small strain. We refer to [43] for the general case. Any plane with normal $\boldsymbol{n}^{\mathrm{p}}$ in the reference configuration as shown in Fig.3 a) can be expressed in this local coordinate systems as

$$\boldsymbol{n}^{\mathrm{p}} = n_1^{\mathrm{p}}\boldsymbol{n}_1 + n_2^{\mathrm{p}}\boldsymbol{n}_2 + n_3^{\mathrm{p}}\boldsymbol{n}_3 \qquad \text{Eq. 16}$$

The possible opening plane is called the potential cracking plane $\boldsymbol{n}^{\mathrm{P}}$. The normal $\boldsymbol{n}^{\mathrm{P}}$ can be also expressed in the form of $(1, \theta^{\mathrm{p}}, \emptyset^{\mathrm{p}})$, so

$$\theta^{\mathrm{p}} = \arctan\left(\frac{n_2^{\mathrm{P}}}{n_1^{\mathrm{P}}}\right) \qquad \text{Eq. 17}$$

$$\emptyset^{\mathrm{p}} = \arcsin(n_3^{\mathrm{P}}) \qquad \text{Eq. 18}$$

Therefore, with the normal of the potential cracking plane $(1, \theta^{\mathrm{P}}, \emptyset^{\mathrm{P}})$, its effective fracture strength (critical strength) and energy dissipation are:

$$\sigma_{\mathrm{c}} = \sqrt{(\cos\emptyset^{\mathrm{P}}\cos\theta^{\mathrm{P}}\,\sigma_{\mathrm{c}}^{1})^2 + (\cos\emptyset^{\mathrm{P}}\sin\theta^{\mathrm{P}}\,\sigma_{\mathrm{c}}^{2})^2 + (\sin\emptyset^{\mathrm{P}}\,\sigma_{\mathrm{c}}^{3})^2} \qquad \text{Eq. 19}$$

$$G_{\mathrm{c}} = \sqrt{(\cos\emptyset^{\mathrm{P}}\cos\theta^{\mathrm{P}}\,G_{\mathrm{c}}^{1})^2 + (\cos\emptyset^{\mathrm{P}}\sin\theta^{\mathrm{P}}\,G_{\mathrm{c}}^{2})^2 + (\sin\emptyset^{\mathrm{P}}\,G_{\mathrm{c}}^{3})^2} \qquad \text{Eq. 20}$$

The effective cohesive stress is defined as [31]:

$$\sigma_{\text{eff}} = \begin{cases} \sqrt{(\sigma_{\text{n}})^2 + \beta^{-2}(\sigma_{\tau})^2}, & \sigma_{\text{n}} \geq 0 \\ \frac{1}{\beta} \ll |\sigma_{\tau}| - \eta|\sigma_{\text{n}}| \gg, & \sigma_{\text{n}} < 0 \end{cases} \quad \text{Eq. 21}$$

where $\sigma_{\text{n}} = \overline{\boldsymbol{n}} \cdot \boldsymbol{t}$ and $\sigma_{\tau} = \sqrt{\boldsymbol{t} \cdot \boldsymbol{t} - (\sigma_{\text{n}})^2}$ are respectively the normal and shear components of the surface traction $\boldsymbol{t}$ on the interface, and $\beta = \text{K}_{\text{IC}}/\text{K}_{\text{IIC}}$ (K_{IC} and K_{IIC} are the fracture toughness parameters of mode I and II, so β assigns the different weights to the two modes) and η is the friction coefficient.

The stress on a surface with normal $\boldsymbol{n}^{\text{P}}$ is:

$$\boldsymbol{\sigma}^{\text{P}} = \boldsymbol{\sigma}^{\text{L}} \cdot \boldsymbol{n}^{\text{P}} \quad \text{Eq. 22}$$

where $\boldsymbol{\sigma}^{\text{L}}$ is the stress in the local coordinate system. So:

$$\begin{aligned} \sigma_1^{\text{P}} &= \sigma_{11}^{\text{L}} \cos\emptyset^{\text{P}} \cos\theta^{\text{P}} + \sigma_{12}^{\text{L}} \cos\emptyset^{\text{P}} \sin\theta^{\text{P}} + \sigma_{13}^{\text{L}} \sin\emptyset^{\text{P}} \\ \sigma_2^{\text{P}} &= \sigma_{21}^{\text{L}} \cos\emptyset^{\text{P}} \cos\theta^{\text{P}} + \sigma_{22}^{\text{L}} \cos\emptyset^{\text{P}} \sin\theta^{\text{P}} + \sigma_{23}^{\text{L}} \sin\emptyset^{\text{P}} \\ \sigma_3^{\text{P}} &= \sigma_{31}^{\text{L}} \cos\emptyset^{\text{P}} \cos\theta^{\text{P}} + \sigma_{32}^{\text{L}} \cos\emptyset^{\text{P}} \sin\theta^{\text{P}} + \sigma_{33}^{\text{L}} \sin\emptyset^{\text{P}} \end{aligned} \quad \text{Eq. 23}$$

And then the normal stress $\sigma_{\text{n}}^{\text{P}}$ and shear stress σ_{τ}^{P} on the potential plane are:

$$\sigma_{\text{n}}^{\text{P}} = \sigma_1^{\text{P}} \cos\emptyset^{\text{p}} \cos\theta^{\text{p}} + \sigma_2^{\text{P}} \cos\emptyset^{\text{p}} \sin\theta^{\text{p}} + \sigma_3^{\text{P}} \sin\emptyset^{\text{p}} \quad \text{Eq. 24}$$

$$\sigma_{\tau}^{\text{P}} = \sqrt{\|\boldsymbol{\sigma}^{\text{P}}\|^2 - (\sigma_{\text{n}}^{\text{P}})^2} \quad \text{Eq. 25}$$

With Eq. 21, 24 and 25, the effective cohesive stress $\sigma_{\text{eff}}(\theta^{\text{P}}, \emptyset^{\text{P}})$ on the potential cracking plane can be obtained. Notice that as shown in Fig.3 b), as limited by the meshes, the potential cracking plane can only be partly represented by the element interface. When the effective cohesive stress σ_{eff} reaches the critical strength $\sigma_{\text{c}}(\theta^{\text{P}}, \emptyset^{\text{P}})$ on one potential cracking plane, the crack is initiated, and the crack will open at the element interface. Obviously, the potential cracking plane which can be partly represented by the element interface should not be orthogonal to the element interface.

For the special case of unidirectional (UD) composites, $\sigma_{\text{c}}^1 = \sigma_{\text{c}}^2 = \sigma_{\text{c}}^{\text{T}}$ and $G_{\text{c}}^1 = G_{\text{c}}^2 = G_{\text{c}}^{\text{T}}$. $\sigma_{\text{c}}^{\text{L}}$ and G_{c}^{L} are respectively the critical stress and energy dissipation rate for the longitudinal fracture, and $\sigma_{\text{c}}^{\text{T}}$ and G_{c}^{T} are respectively the critical stress and energy dissipation rate for the transverse fracture. Because of their transverse isotropic behaviours, the critical stress and energy dissipation from Eq. 19 and 20 can then be simplified as:

$$\sigma_{\text{c}}(\emptyset^{\text{P}}) = \sqrt{(\cos\emptyset^{\text{P}}\, \sigma_{\text{c}}^{\text{T}})^2 + (\sin\emptyset^{\text{P}}\, \sigma_{\text{c}}^{\text{L}})^2} \quad \text{Eq. 26}$$

$$G_{\text{c}}(\emptyset^{\text{P}}) = \sqrt{(\cos\emptyset^{\text{P}}\, G_{\text{c}}^{\text{T}})^2 + (\sin\emptyset^{\text{P}}\, G_{\text{c}}^{\text{L}})^2} \quad \text{Eq. 27}$$

Assuming the crack should not follow the finite element interfaces, it can be assumed that there are only two physically possible crack propagation directions – the transverse and longitudinal. Therefore, the crack initiation only needs to be checked on the surfaces with $\emptyset^{\mathrm{P}} = 0$ or $\pi/2$.

For $\emptyset^{\mathrm{P}} = 0$, from Eq. 24 and 25, we have:

$$\sigma_{\mathrm{n}}^{\mathrm{P}} = \sigma_1^{\mathrm{P}} \cos\theta^{\mathrm{P}} + \sigma_2^{\mathrm{P}} \sin\theta^{\mathrm{P}} \quad \text{Eq. 28}$$

$$\sigma_{\tau}^{\mathrm{P}} = \sqrt{\|\boldsymbol{\sigma}^{\mathrm{P}}\|^2 - (\sigma_{\mathrm{n}}^{\mathrm{P}})^2} \quad \text{Eq. 29}$$

So, the crack is initiated when $\max\{\sigma_{\mathrm{eff}}(\theta^{\mathrm{P}})\} = \sigma_{\mathrm{c}}^{\mathrm{T}}$.

For $\emptyset^{\mathrm{P}} = \pi/2$, from Eq. 24 and 25, we have:

$$\sigma_{\mathrm{n}}^{\mathrm{P}} = \sigma_3^{\mathrm{P}} \quad \text{Eq. 30}$$

$$\sigma_{\tau}^{\mathrm{P}} = \sqrt{(\sigma_1^{\mathrm{P}})^2 + (\sigma_2^{\mathrm{P}})^2} \quad \text{Eq. 31}$$

Then the crack initiation criterion is

$$\sigma_{\mathrm{c}}^{\mathrm{L}} = \begin{cases} \sqrt{(\sigma_3^{\mathrm{P}})^2 + \beta^{-2}((\sigma_1^{\mathrm{P}})^2 + (\sigma_2^{\mathrm{P}})^2)}, & \sigma_3^{\mathrm{P}} \geq 0 \\ \frac{1}{\beta} \ll \sqrt{(\sigma_1^{\mathrm{P}})^2 + (\sigma_2^{\mathrm{P}})^2} - \eta\left|\sigma_3^{\mathrm{P}}\right| \gg, & \sigma_3^{\mathrm{P}} < 0 \end{cases} \quad \text{Eq. 32}$$

2.3.2 Intralaminar fracture propagation along interface elements

With the DG code, cracks are constrained to follow interface elements of normal $\bar{\boldsymbol{n}}$, in the reference configuration as shown in Fig.3 b). We then assume that $\boldsymbol{n}^{\mathrm{p}} = \bar{\boldsymbol{n}}$, with $\bar{\theta} = \arctan\left(\frac{\bar{n}_2}{\bar{n}_1}\right)$ and $\bar{\emptyset} = \arcsin(\bar{n}_3)$.

Therefore, one has as critical energy release rate

$$G_{\mathrm{c}}^{\mathrm{e}} = G_{\mathrm{c}}\left(\bar{\emptyset}\right) \quad \text{Eq. 33}$$

and then the critical opening as shown in Fig.4 is

$$\Delta_{\mathrm{c}}^{\mathrm{e}} = 2G_{\mathrm{c}}^{\mathrm{e}}/\sigma_{\mathrm{c}}^{\mathrm{e}} \quad \text{Eq. 34}$$

where $\sigma_{\mathrm{c}}^{\mathrm{e}}$ is computed on the element interface by Eq. 21 at the time step of the crack onset when $\sigma_{\mathrm{eff}} = \sigma_{\mathrm{c}}\left(\bar{\emptyset}\right)$. The two terms $\sigma_{\mathrm{c}}\left(\bar{\emptyset}\right)$ and $G_{\mathrm{c}}\left(\bar{\emptyset}\right)$ are evaluated from respectively Eq. 26 and Eq. 27.

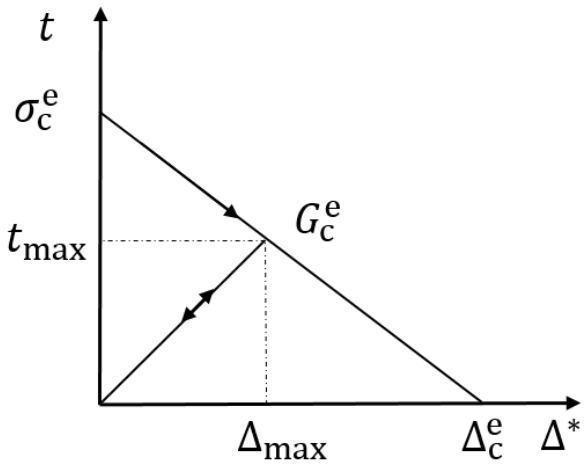

Fig.4 Linear extrinsic cohesive law for the intralaminar fracture

The effective surface opening Δ^* of the element interface is calculated from the surface opening vector $\overline{\boldsymbol{u}}$ by:

$$\Delta^* = \sqrt{\ll \Delta_n^* \gg^2 + \beta^2 (\Delta_\tau^*)^2} \qquad \text{Eq. 35}$$

where, $\Delta_n^* = \overline{\boldsymbol{u}} \cdot \overline{\boldsymbol{n}}$ and $\Delta_\tau^* = \sqrt{\|\overline{\boldsymbol{u}}\|^2 - (\Delta_n^*)^2}$.

The linear extrinsic cohesive law used in this work includes an irreversible softening part during the interface opening and, also a reversible part only if the opened interface is unloaded. Then the effective cohesive traction t can be calculated by:

$$t = \begin{cases} \sigma_c^e \left(1 - \frac{\Delta^*}{\Delta_c^e}\right), & \dot{\Delta}^* \geq 0 \text{ and } \Delta^* = \Delta_{max} \\ t_{max} \frac{\Delta^*}{\Delta_{max}}, & \dot{\Delta}^* < 0 \text{ and } \Delta^* < \Delta_{max} \end{cases} \qquad \text{Eq. 36}$$

Finally based on this TSL, the surface traction $\boldsymbol{t}$ can be evaluated as a function of the effective cohesive traction t by:

$$\boldsymbol{t} = \begin{cases} t\left(\frac{\Delta_n^*}{\Delta^*}\overline{\boldsymbol{n}} + \beta \frac{|\Delta_\tau^*|}{\Delta^*}\overline{\boldsymbol{\tau}}\right), & \sigma_n \geq 0 \\ t\beta \frac{|\Delta_\tau^*|}{\Delta^*}\overline{\boldsymbol{\tau}}, & \sigma_n < 0 \end{cases} \qquad \text{Eq. 37}$$

where, $\overline{\boldsymbol{\tau}}$ is the interface tangent in the deformed configuration.

3. Numerical simulations and validations

In this section the energy absorption behaviour of composite tube specimens is investigated first by quasi-static crushing tests. Then the corresponding simulations have been done and compared to the test results.

3.1 Experiments

3.1.1 Specimens and setup

The carbon/epoxy composite tube used in this work are supplied by Honda R&D Co., Ltd. and produced by Mitsubishi Chemical Corporation. All composite tube specimens are made of Pyrofil™ TR/361 carbon/epoxy in a UD (TR 361E250S) variant. In this material system, the Pyrofil TR 50S15L is a pan based carbon fibre, which is made of non-textile precursor designed for high performance applications. The composite tubes with the TR 50S15L carbon fibre and #361 epoxy were autoclaved for 60 minutes (with a temperature increase of 2 °C/min) at a temperature of 130 °C and a pressure of 0.6 MPa.

To investigate the crushing failure mechanisms of composites, the progressive crush is preferred, so the t/D (thickness/outer diameter) ratio is set in the range 0.015 to 0.25 [44][45]. Based on this design, layups 0/90 and ±45 are considered to obtain different failure patterns of the composite tubes during the crushing process. Here 0 layup indicates the fibre orientation along the axial direction of the tube. The profile of the tube specimen is shown in Table 1. Besides, to reduce the peak load, 45° chamferings were cut on the crushing contact side of each tube specimen.

Table 1 Profile of tube specimen

Inner Diameter	Length	Thickness	Layups
40 mm	40 mm	1.816 mm (8 layers)	$[0/90]_{2s}$, $[\pm45]_{2s}$

All tests have been performed with the test bench-Instron 5885H in the quasi-static constant loading speed 10mm/min. The final crushing displacement for the axial loading test was set to be 5 mm, and the crushing force and displacement data of the loading part were recorded.

3.1.2 Test results

During the crushing process, different kinds of failure patterns have been observed, including delamination, axial crack propagation, petals bending, fracture of fibres and matrices. Among the above failure patterns, the most visible differences of the two layups of tube specimens are the crack propagations as shown in Fig.5. The directions in which the cracks propagate in the tube specimens are classified into 2 modes: 1) $[0/90]_{2s}$: clear debonding between outer petals and inner petals and crack propagation along the axial direction in 0 degree layer; 2) $[\pm45]_{2s}$: crack propagation in 45 degrees causing the screw petals.

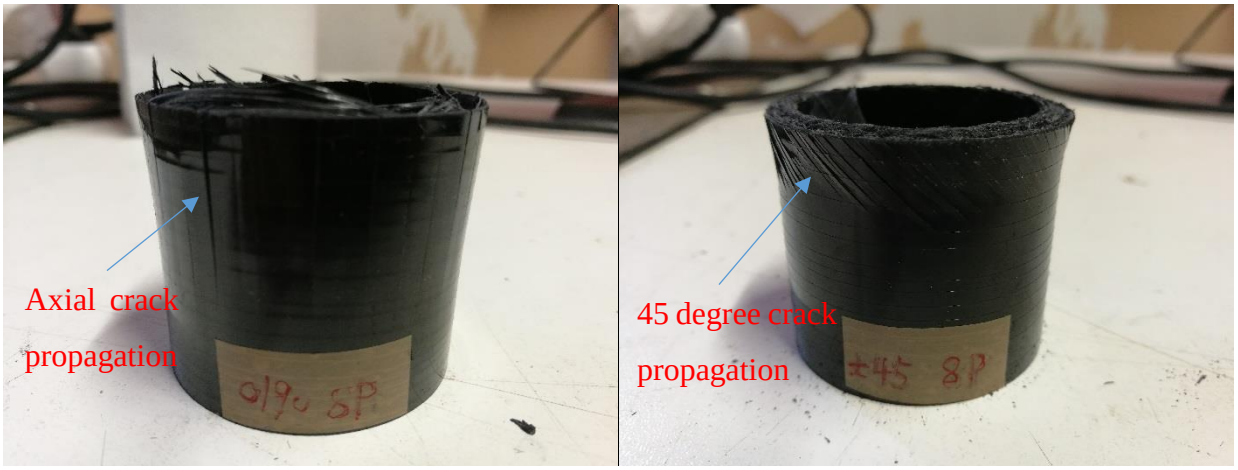

a) Mode 1 b) Mode 2

Fig.5 Different crack modes in layup 0/90 and ±45

The performance of energy absorbing structures can be described by their specific energy absorption (SEA), peak crush load (F_{P}), average crush load (F_{A}) and crush efficiency (CE). The energy absorption is the energy absorbed by the structure during the crushing process. To fairly evaluate the energy absorption ability of different structures, the specific energy absorption (SEA) has been adopted, which is defined as:

$$\mathrm{SEA} = \frac{\int_0^{l_{max}} F(l)dl}{\rho l_{max}} \ (\mathrm{kJ/kg}) \qquad \text{Eq. 38}$$

where ρ is the linear density of the tube specimens, $F(l)$ is the instantaneous crush load corresponding to the instantaneous crushing deformation length (the instantaneous displacement of the impactor), and l_{max} is the total crushed length. A higher SEA value indicates a better crush energy absorption capacity of the structure.

To evaluate the energy absorption of the rest part after the first contact, the ratio of the average crush load F_{A} to the peak crush load F_{P} is adopted and identified as the crush efficiency (CE). The average crush load (F_{A}) is defined as:

$$F_{\mathrm{A}} = \frac{\int_0^{l_{max}} F(l)dl}{l_{max}} \ (\mathrm{kN}) \qquad \text{Eq. 39}$$

With the same energy absorption, a lower CE means normally a higher peak crush load F_{P} and as well as a lower average crush load F_{A}, and hence a catastrophic crush failure. A higher CE indicates a more progressive crush failure. The quasi-static test results of the SEA and CE values are summarized in Table 2.

Table 2 Quasi-static test results

Test ID	Max Load (kN)	Ave Max Load (kN)	SEA (kJ/kg)	Ave SEA (kJ/kg)	CE (-)	Ave CE (-)
UD090C8P_1	27.87		36		48%	
UD090C8P_2	26.35	26.62	35	36	46%	49%
UD090C8P_3	25.63		37		51%	
UD45C8P_1	21.62		26		44%	
UD45C8P_2	18.26	20.03	27	27	38%	41%
UD45C8P_3	20.22		27		40%	

Note: UD -- Unidirectional

3.2 Modelling

3.2.1 DG crush model with stacked solid element layers

The DG/CZM model of the carbon/epoxy tube is generated by the above methods and illustrated in Fig.6. Considering the axial symmetry, a quarter model is used for computation efficiency. The first order prism element (linear 6-node triangular prism element with 18 degrees of freedom) is used in this model. The dimensions of the tube model are the same as the tube specimens (length 40 mm, inner diameter 40 mm, thickness of each layer 0.227 mm), and the 8-layers DG/CZM model with 45° chamfering on the top is created. The interfaces between each two layers are modelled with the mixed mode extrinsic cohesive law. The upper impact loading plate is modelled by a rigid surface, and the bottom of the quarter tube is fixed. Symmetric boundary conditions (fix the normal displacement, which is perpendicular to the two side surfaces where the symmetric boundary condition is applied on, as shown in Fig.6) are applied on the two sides of the quarter tube model.

A much higher loading velocity is adopted instead of the actual one 10 mm/min to accelerate the computation process. A reasonable loading velocity should lead to a global response of the structure which is the same as in the static/quasi-static case. However, in fracture mechanics, the fracture damage is a rather local behaviour. To investigate the effects of the loading velocity in this model, three loading velocities equal to 10m/s, 20m/s and 30 m/s have been applied. The three different loading velocities are applied to the layup $[-45/+45]_{2s}$ to check their effects on the simulation results. As shown in Fig.6, the mesh sizes are increasing from the top to the bottom. The crush length in the simulation is set as the same 5 mm as that in the test, so more fracture failure patterns can be expected in the crush region (around 16 mm height) which covers the 5 mm crush length. In this crush region, the refined average mesh size is about 1 mm.

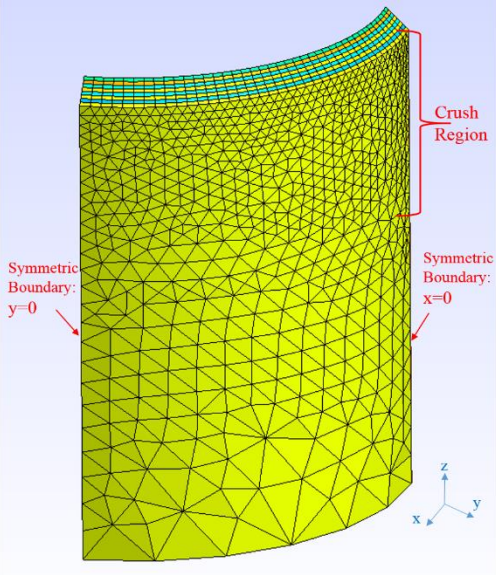

Fig.6 6-node prism solid element meshes of a quarter part of the composite tube with 8 layers

3.2.2 Material properties

The composite layers of the tube specimens are considered to be linear elastic and transversely isotropic, so the 3D material model used in this work has only 5 independent material parameters E_3, E_1, G_{31}, ν_{31} and ν_{12} for the elastic behaviour before damage in the 3D constitutive law, which are listed in Table 3. In our model, the longitudinal direction (the fibre orientation) is direction 3, and the two symmetric transverse directions are directions 1 and 2. The details of the transverse isotropic constitutive law are presented in the Appendix A. The all material properties used in this model are reported in Table 3.

Table 3 Material properties

Description		Variable	Value
Density (kg/m^3)		ρ	1574 *
Elastic property (GPa)		E_3 E_1 G_{31}	126 * 9.4 [46] 4.1 *
Poisson ratio (-)		υ_{31} υ_{12}	0.31 * 0.42 ⋄
Interlaminar fracture properties	Critical stress (MPa)	σ_{IC} σ_{IIC}	71 † 71 △

	Energy dissipation rate (N/mm)	G_{IC} G_{IIC}	0.104 [47] 0.208 △
Intralaminar fracture properties	Critical stress (MPa)	σ_c^L σ_c^T	3186 ◇ 71 †
	Energy dissipation rate (N/mm)	G_c^L G_c^T	54 □ 0.277 ■

* Test data TR 360E250S unidirectional carbon/epoxy composite laminates.

◊ R.D.B. Sevenois et al. 2018, MESI approach [48].

† Data tension test on the pure #360 epoxy specimen.

△ σ_{IC} is taken equal to σ_{IIC} ([41] [49]), and G_{IIC} is assumed as twice of G_{IC} ([41]).

◇ Tension strength of the TR 50S15L carbon fibre [50] is multiplied with the volume fraction 65% (the volume fraction is obtained from the measurement and simulation on the TR 360E250S unidirectional carbon/epoxy composite laminates).

□ Data estimated from the energy dissipation rate corresponding to the fibre tensile failure of T300/920 carbon/epoxy measured by Laffan et al. [51][52].

■ G_c^T is a mean value of different Bisphenol-A type epoxies' values reported in reference [49]. Here this value is considered as a typical value of epoxy's energy dissipation rate.

Because the carbon fibre is much stronger than the matrix, the crack prefers to propagate in the matrix as observed in crushing tests. Therefore, for the transverse fracture (as shown in Fig.7 a)), both the critical stress and energy dissipation rate are the same as those of the matrix. For the longitudinal fracture (as shown in Fig.7 b)), the critical stress σ_c^L is dominated by the fibre. Because the energy dissipation rate of a single carbon fibre can be as low as 7.4 J/m^2 [53], the energy is mostly dissipated in this failure mode by the fibre-matrix debonding and subsequent fibre pull-out [52]. The T300 and TR 50S15L carbon fibre have similar tensile modulus (230GPa and 240GPa), and the two epoxy matrices with prepreg are cured in similar conditions (1 hour at 125°C with 0.3MPa pressure and 1 hour at 130°C with 0.6MPa pressure). Therefore, the G_c^L used in this work is assumed from the energy dissipation rate corresponding to the fibre tensile failure of the T300/920 carbon/epoxy composite [51][52].

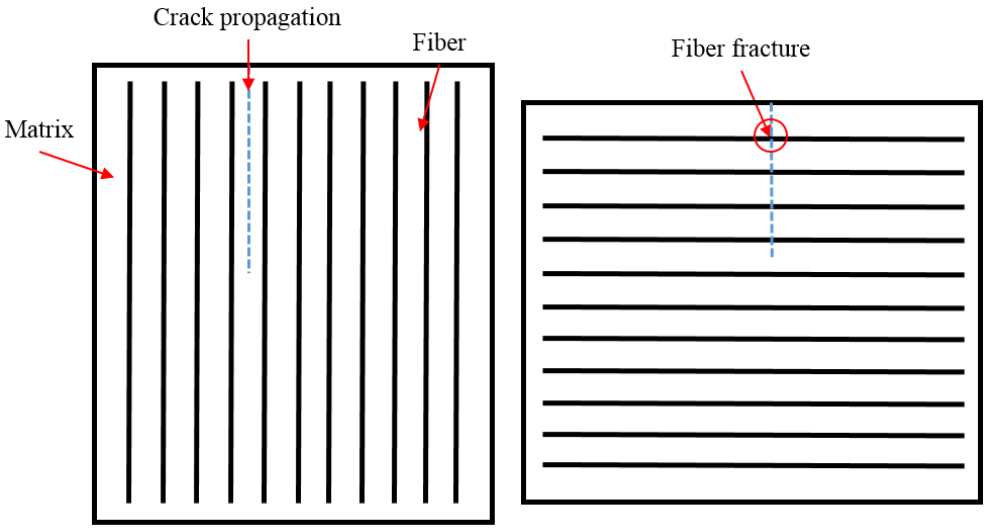

a)Transverse fracture b)Longitudinal fracture

Fig.7 Intra-laminar fracture directions

3.3Results and discussion

3.3.1 Results of different loading velocities

As shown in Fig.8, the predicted peak loads change with the increase of the loading velocity. The increase of the loading velocity doesn't highly affect the peak load in this case. This is maybe due to the elastic behaviour used in this model, and the peak load is mainly identified by the strength of the material which is not changed with different loading velocities. Also notice that with the highest loading velocity 30 m/s, there are more peaks observed in the curve, which cannot represent the behaviour observed in the test.

The time step in the explicit computation process is defined by the mesh size and stiffness of the materials. Within the same mesh size and material properties, the higher loading velocity can faster reach the expected crush length. Therefore, considering the balance between the computation efficiency and the influence of the loading speed, the loading speed of 20 m/s is chosen as the used one in this work.

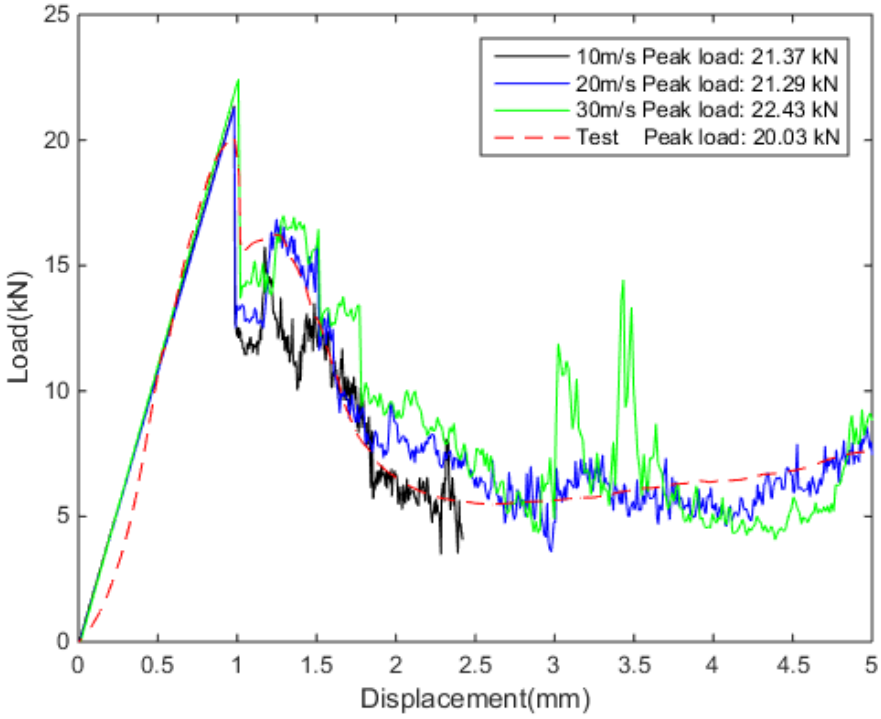

Fig.8 Load-displacement history of composite tubes with layup $[+45/-45]_{2s}$ from the simulations test in different loading speeds

(The value of the peak load is the average value of 3 repetition as listed in Table 2, and the load-displacement curve shown is a typical result from a single test)

For the $[+45/-45]_{2s}$ tube, the material properties are not fully axial-symmetric. Indeed, there are some local responses in the tube model which are introduced by the boundary conditions and different from the test results. However, the effect introduced by the boundary conditions stays local. Considering the global response as shown in Fig.8, for the $[+45/-45]_{2s}$ tube in this case, the tube can still be approximately simulated by a quarter model.

3.3.2 Results of different layups

The simulations above were running with 90 partitions for 10 days for each. As shown in Fig.9 and Fig.10 (in the figures, the SEA and CE values are the average ones as listed in Table 2, and the curves are typical ones chosen from one of the 3 repetitions for each layup), the peak loads of the simulations are close to those of the tests both in case of layup $[0/90]_{2s}$ and $[+45/-45]_{2s}$. This means that the used DG/CZM model can predict the peak load of the crushing process. As shown in Fig.11 a) and Fig.14 a), the first damage in both layups $[0/90]_{2s}$ and $[+45/-45]_{2s}$ is the delamination, which is the same as what was observed in the tests and reported in the literature

[44]. Therefore, the strength of the interface between layers dominates the peak crush load during the crushing process.

Because in real practice, the used mesh in the model can't be arbitrary fine, when the coarse mesh can't provide enough possible crack propagation path, badly distorted elements may apparent and hurt the stability of simulation. Therefore, element erosion technique is used to avoid this numerical problem. The used element erosion technique is based on the SVM (Stress Von Mises) value to delete those distorted elements. The simulation result visualization is based on an open source program GMSH [54]. To avoid showing the strange distorted elements, the deformed tube models in a custom-chosen configuration in GMSH with a limit range of SVM values are shown in Fig.11~15. As the SVM value is not meaningful for anisotropic materials, the colour distribution in the figures is only for indication. The metrics for validating the model are the peak load, SEA, crush efficiency and the numerical crack length. As illustrated in Fig.9 and 10, the simulation SEA and crushing efficiency values are quite close to the test results.

The oscillations observed in the simulation results firstly come from the explicit time integration although numerical damping is used [41][55]. Then as mentioned above, the element erosion is used in this model to delete the distorted elements. The eroded elements mostly occur where the rigid loading plate directly touches. This leads to the response force reductions in the crush load history, which is shown in the history as the oscillations. However, as shown in Fig.8~10, with this model and mesh size, the main energy absorption behaviour (peak load, energy absorption value and crushing efficiency) of the composite tube can be predicted accurately.

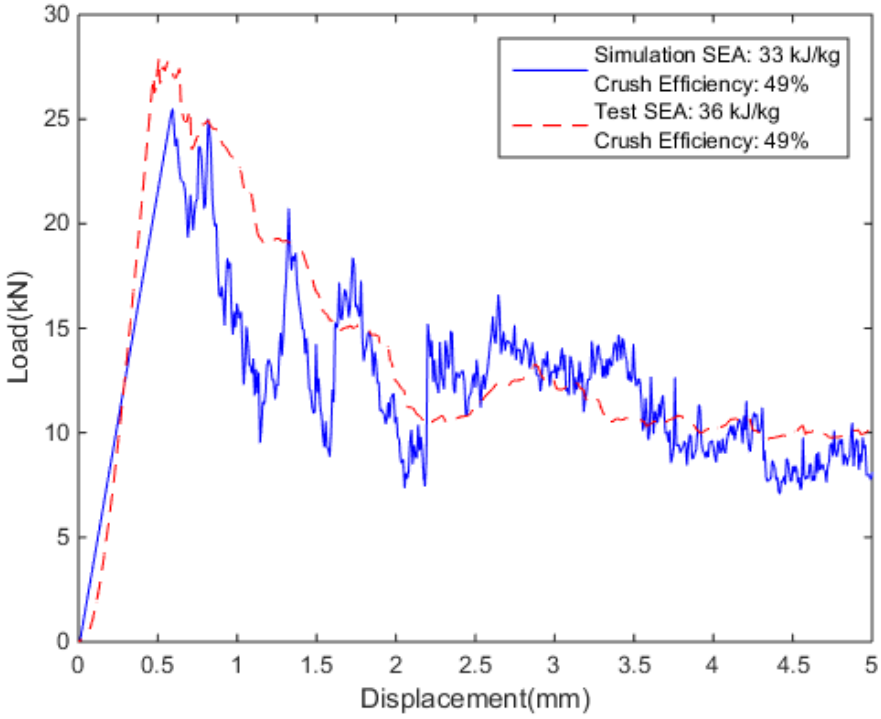

Fig.9 Load-displacement history of $[0/90]_{2s}$ composite tubes from the test and simulation

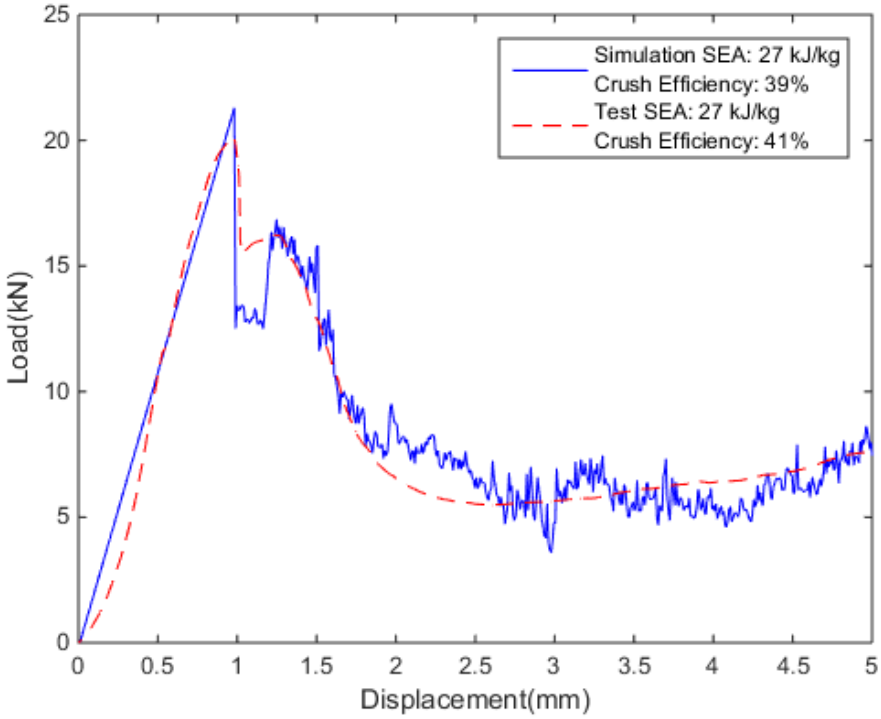

Fig.10 Load-displacement history of $[+45/-45]_{2s}$ composite tubes from the test and simulation

As shown and marked in red in Fig.12, Fig.13 and Fig.15, different crack propagations are observed, which are controlled by the anisotropic cohesive laws in the model. The cracks stop at the transition of fine mesh to coarse mesh, firstly it is because the cracks have already reached the length for the energy dissipation. The crack lengths predicted by the model are comparable to the crack lengths observed in the tests (as shown in Fig.12: simulation crack length – 16.5 mm and test crack length – 17 mm; in Fig.15 a): simulation crack length – 10 mm and test crack length – 10.5 mm). This demonstrates the capacity of the DG model with ACEL for capturing the potential crack propagations during the crushing process. Secondly, since further crack propagation will occur at big element interface, and the opening at interface of big element will need more energy dissipation. In the limited loading distance, this energy can't be provided for crack propagation anymore. However, the simulation crack length is already comparable to the test crack length in the crush region, so the crack propagation in the rest part is not significant and the coarse mesh used in this part can accelerate the computation. Therefore, in this DG/ACEL model, a suitable crush region with fine mesh and the rest part with coarse mesh can balance the simulation accuracy and efficiency. The influences of the size and shape of the mesh can be respectively summarized as follows:

1) Because the crack propagations are constrained on the interface of the elements, the mesh size should be fine enough to have enough element interfaces, which can reproduce all possible crack propagations in the tests to keep this model predictive. Because the damage simulation is only calculated in the cohesive model with the element interfaces, the response of the solid element is always elastic based on the elastic anisotropic constitutive law. Therefore, coarse meshes in the stress concentration region may lead the solid elements to be distorted, which would cause the negative Jacobian problem. As a conclusion, in the crush region/stress concentration region, fine meshes are used to reproduce the crush damage, and the coarser meshes in the rest part are used to balance the computation cost.

2) As discussed in Section 2.3 and illustrated in Fig.3 b), the element interface doesn’t always represent the true cracking plane. The true cracking plane is identified by the crack initiation criterion presented in Section 2.3.1. Then the opened element interface is the one which is closest to the true cracking plane, and the relation between the energy dissipation on opened element interface and the energy dissipation on the true cracking plane is presented in Section 2.3.2. Therefore, the numerical crack path can represent the main trend of the crack propagation, and will

converge to the real crack path with the decreasing of mesh size, and the energy dissipation as well. Therefore, the shape of the mesh doesn't affect the correct damage simulation, but only visualizes the crack propagation. However, to keep the model predictive and avoid the crack propagation to be overestimated, non-structural meshes instead of structural meshes are recommended in this DG/ACEL method.

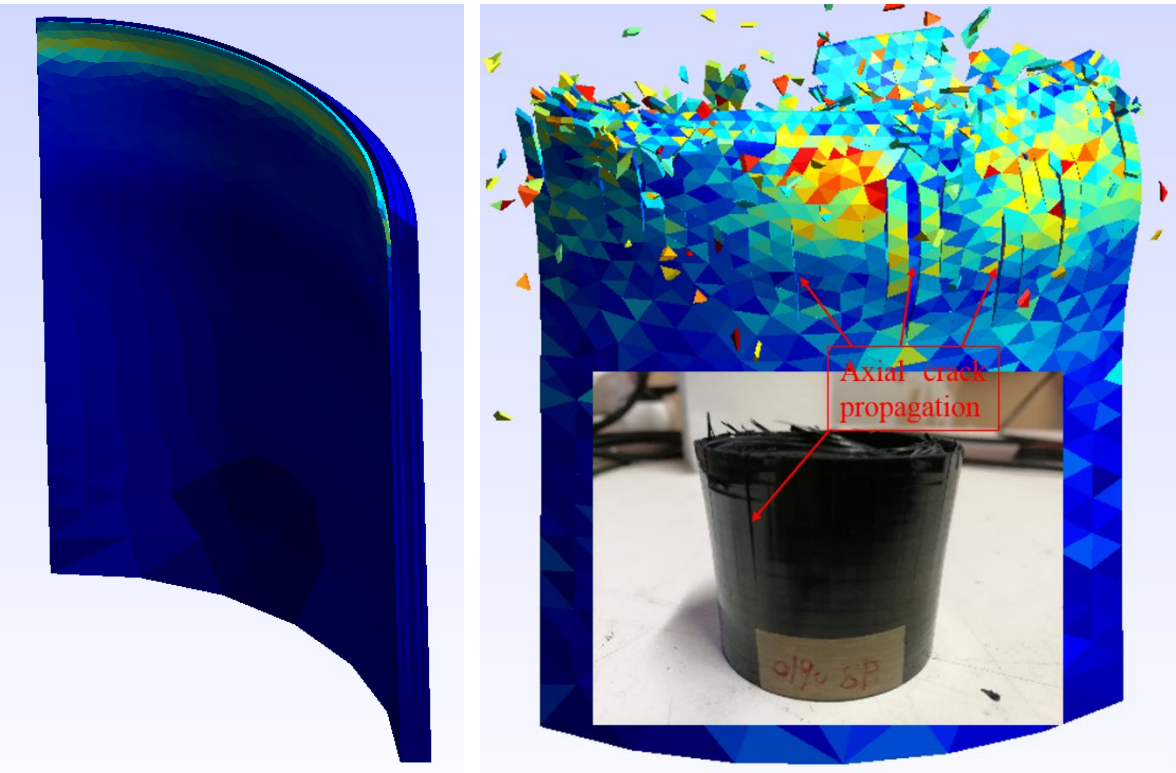

a) Initial damage (delamination) b) Axial cracks in the outer layer

Fig.11 Deformation patterns in the tube model with the layup $[0/90]_{2s}$

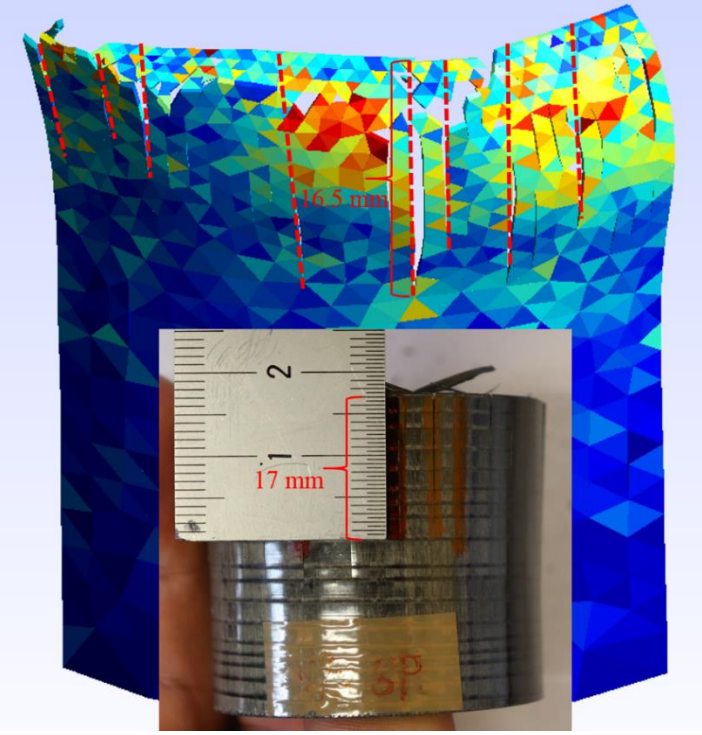

Fig.12 Crack propagation in the tube model in the outer layer with layup 0

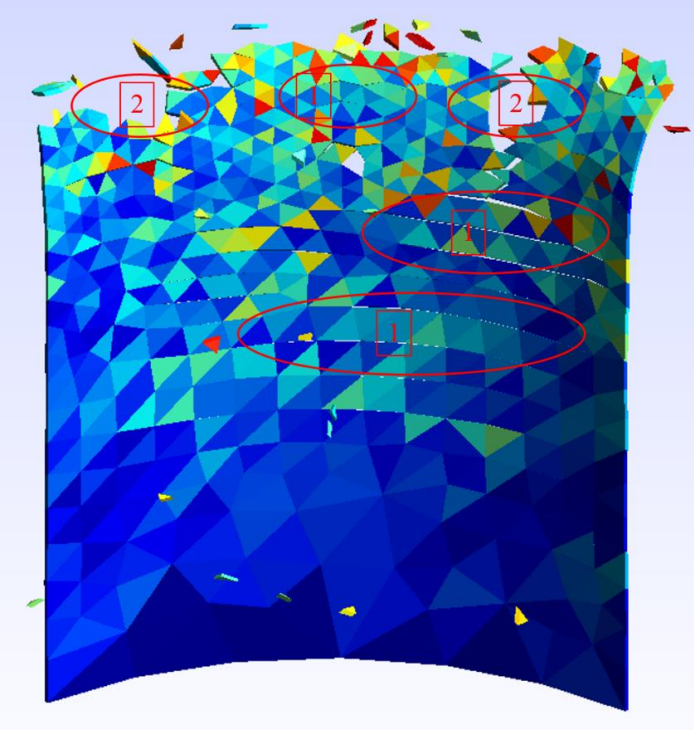

1: Crack propagates in the matrix along the circumferential direction

2: Fibre breakage (these parts are destroyed in this macro level view)

Fig.13 Crack propagation in the tube model in the outer second layer with layup 90

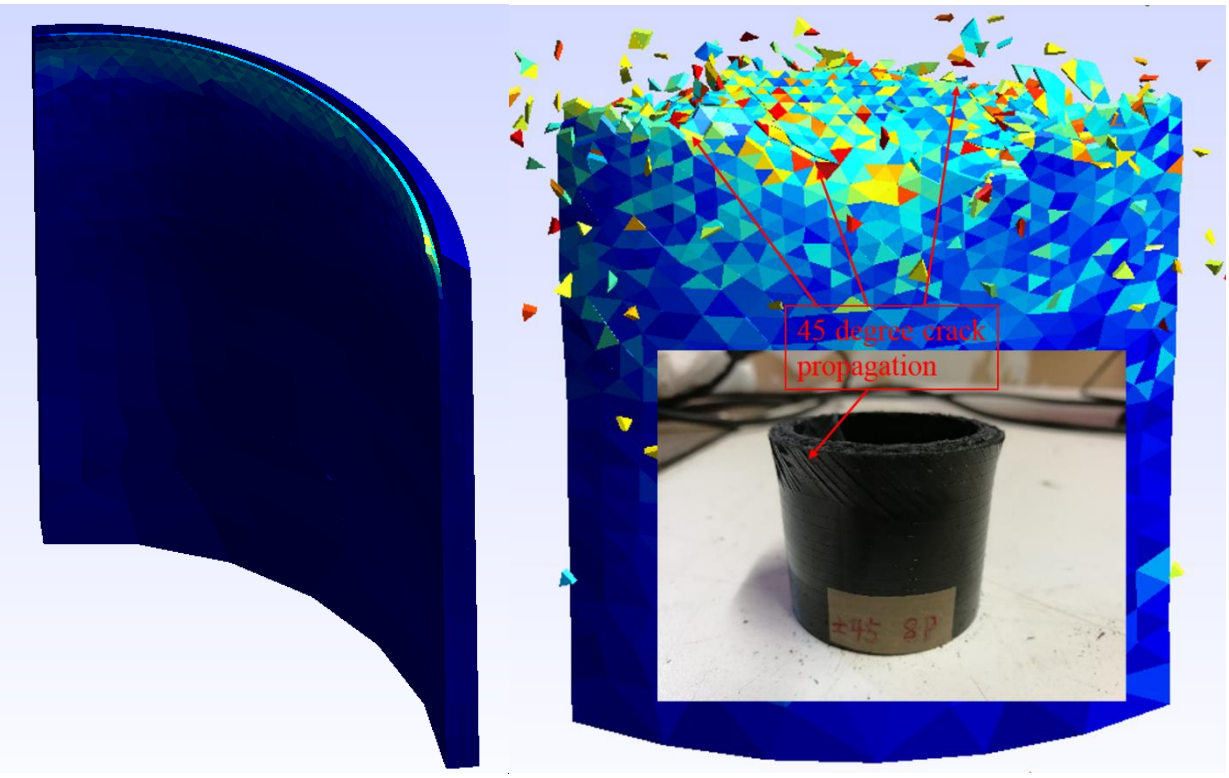

a) Initial damage (delamination) b) Screw crack in the outer layer

Fig.14 Deformation patterns in the tube model with the layup $[+45/-45]_{2s}$

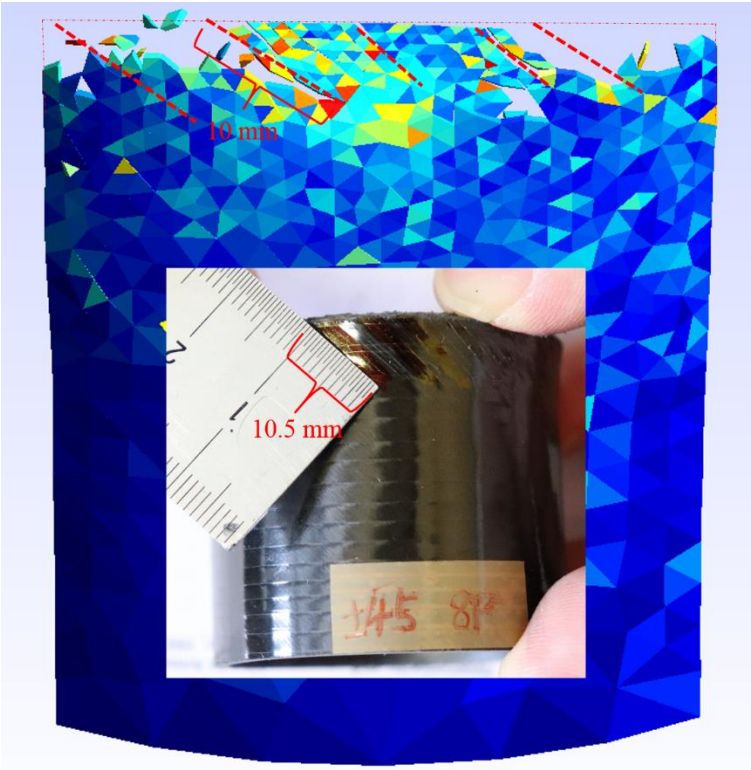

a) +45 layup (outer layer)

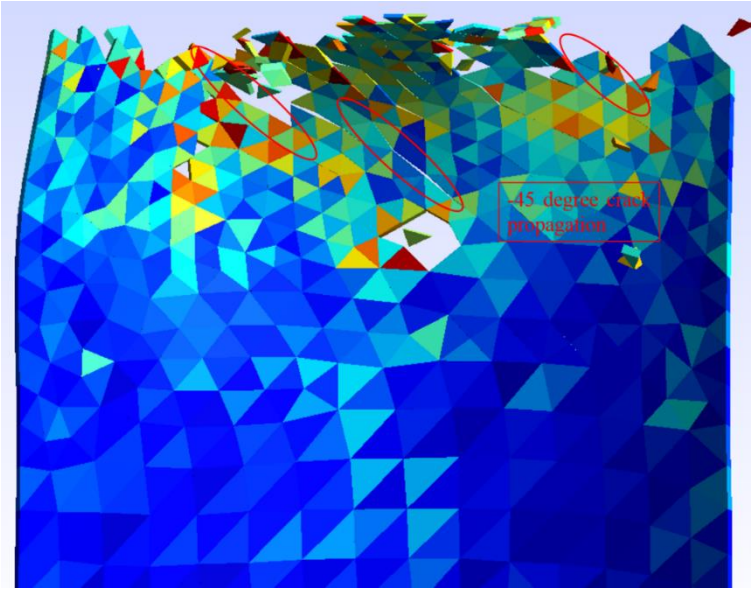

b) -45 layup (inner second layer)

Fig.15 Crack propagation in the tube model in the inner first and second layers

4. Conclusions

This study uses the explicit Discontinuous Galerkin method to simulate the quasi-static crushing process of tube specimens. The mixed mode extrinsic cohesive law is used to simulate the delamination on the interfaces between each layer. To satisfy the different crack modes in different layups, the anisotropic cohesive law is used in the DG method. With a suitable loading speed (20 m/s in this case), which balances the computation efficiency and prediction accuracy, the 8 layers stacked solid element model is capable of reproducing the experimental results with relatively high accuracy.

The differences between the SEAs from the test and the simulation in layup $[0/90]_{2s}$ and $[+45/-45]_{2s}$ are up to around 8%. Palanivenu et al. [16][56] used shell elements for the layer and intrinsic cohesive laws for the delamination between layers, with which the energy absorption has a difference between the tests and simulations of around 6%. Zhu, et.al [57] also used stacked shell elements and damage evolution material laws to simulate the quasi-static crushing process on composite tubes and had a SEA difference around 10%. Therefore, the crush damage model with DG/ACEL method can have a comparable accuracy to the literature in the SEA calculation. The DG/ACEL model uses 3D solid elements, and the nodes can be split into multiples in the computation process. Therefore, the DG/ACEL model asks more computation cost than the stacked shell models used in [16][56][57], and has a similar efficiency as the XFEM method.

However, with the interface boundary on the element interface in the DG/ACEL method, the DG/ACEL model can be more easily implemented in a parallel computation, compared to the other methods.

Besides, compared to the stack shell model with seam elements for intralaminar cracks [16][56], without pre-set crack positions, the DG/ACEL model makes the simulation predictive. Compared to the stack shell model with ply damage models [13][14][57], the DG/ACEL model can avoid the problems caused by the combination of two different kinematic representations for interlaminar and intralaminar failures.

Acknowledgements

The work leading to this publication has been funded by the SBO project "M3Strength", which fits in the MacroModelMat (M3) research program, coordinated by Siemens (Siemens PLM software, Belgium) and funded by SIM (Strategic Initiative Materials in Flanders) and VLAIO (Flanders Innovation & Entrepreneurship Agency). The authors gratefully acknowledge the material suppliers Mitsubishi Chemical Corporation and Honda R&D Co., Ltd.

Appendix

A. Anisotropic constitutive law for the large deformation case

In this DG/CZM model, the transverse isotropic material response was specified to present the behaviour of the composites before damage. In the large deformation conditions, the constitutive law is based on the choice of different strain measures and the definition of the work-conjugate stress. In the method in section 2.1, the first Piola-Kirchhoff stress tensor $\mathbf{P}$ is used and its strain measure is the deformation gradient $\mathbf{F}$, with its Jacobian $J = \det(\mathbf{F}) > 0$. The transverse isotropic elastic material is described by the following parameters:

$$E_{\mathrm{L}} = E_3 \neq E_{\mathrm{T}} = E_1 = E_2 \quad \text{A. 1}$$

$$\nu_{\mathrm{LT}} = \nu_{31} = \nu_{32} \neq \nu_{\mathrm{TT}} = \nu_{12} = \nu_{21} \quad \text{A. 2}$$

$$G_{\mathrm{LT}} = G_{31} = G_{32} \quad \text{A. 3}$$

$$G_{\mathrm{TT}} = G_{12} = \frac{E_1}{2(1+\nu_{12})} \quad \text{A. 4}$$

The fibre direction is the direction 3. The composite laminate is modelled by the Neo-Hookean material in the large deformation condition, which has a strain energy density Ψ dependent on the right Cauchy-Green tensor $\mathbf{C} = \mathbf{F}^{\mathbf{T}}\mathbf{F}$. Then the strain energy density Ψ can be calculated separately in two parts [58]:

$$\Psi = \Psi_{\mathrm{iso}} + \Psi_{\mathrm{trn}} \quad \text{A. 5}$$

$$\Psi_{\mathrm{iso}} = \frac{1}{2} G_{\mathrm{TT}}(I_1 - 3) - G_{\mathrm{TT}} \ln J + \frac{1}{2}\lambda \ln^2 J \quad \text{A. 6}$$

$$\Psi_{\mathrm{trn}} = [\alpha_{\mathrm{trn}} + 2\beta_{\mathrm{trn}} \ln J + \gamma_{\mathrm{trn}}(I_4 - 1)](I_4 - 1) - \frac{1}{2}\alpha_{\mathrm{trn}}(I_5 - 1) \quad \text{A. 7}$$

where $I_1 = \mathrm{tr}(\mathbf{C})$, $J^2 = \det(\mathbf{C})$, $I_4 = \mathbf{A} \cdot \mathbf{C} \cdot \mathbf{A}$, and $I_5 = \mathbf{A} \cdot \mathbf{C^2} \cdot \mathbf{A}$. The unit vector $\mathbf{A}$ is in the fiber direction in the undeformed configuration. Besides, other parameters in A. 6 and A. 7 are:

$$\lambda = \frac{E_{\mathrm{T}}(\nu_{\mathrm{TT}} + n\nu_{\mathrm{LT}}^2)}{m(1+\nu_{\mathrm{TT}})} \quad \text{A. 8}$$

$$G_{\mathrm{TT}} = \frac{E_{\mathrm{T}}}{2(1+\nu_{\mathrm{TT}})} \quad \text{A. 9}$$

$$\alpha_{\mathrm{trn}} = G_{\mathrm{TT}} - G_{\mathrm{LT}} \quad \text{A. 10}$$

$$\beta_{\mathrm{trn}} = \frac{E_{\mathrm{T}}[n\nu_{\mathrm{TL}}(1+\nu_{\mathrm{TT}}-\nu_{\mathrm{TL}})-\nu_{\mathrm{TT}}]}{4m(1+\nu_{\mathrm{TT}})} \quad \text{A. 11}$$

$$\gamma_{\mathrm{trn}} = \frac{E_{\mathrm{L}}(1-\nu_{\mathrm{TT}})}{8m} - \frac{\lambda + 2G_{\mathrm{TT}}}{8} + \frac{\alpha_{\mathrm{trn}}}{2} - \beta_{\mathrm{trn}} \quad \text{A. 12}$$

$$m = 1 - \nu_{\mathrm{TT}} - 2n\nu_{TL}^2 \quad \text{A. 13}$$

$$n = \frac{E_{\mathrm{L}}}{E_{\mathrm{T}}} \quad \text{A. 14}$$

Then the second Piola-Kirchhoff stress tensor $\boldsymbol{S}$ can be calculated by differentiating A. 5, A. 6 and A. 7:

$$\boldsymbol{S} = 2\frac{\partial \Psi}{\partial \boldsymbol{C}} = \lambda\, ln J \boldsymbol{C^{-1}} + G_{12}(\boldsymbol{I} - \boldsymbol{C^{-1}}) + 2\beta_{\mathrm{trn}}(I_4 - 1)\boldsymbol{C^{-1}} + 2[\alpha_{\mathrm{trn}} + 2\beta_{\mathrm{trn}}\, ln J + 2\gamma_{\mathrm{trn}}(I_4 - 1)]\boldsymbol{A} \otimes \boldsymbol{A} - \alpha_{\mathrm{trn}}(\boldsymbol{C} \cdot \boldsymbol{A} \otimes \boldsymbol{A} + \boldsymbol{A} \otimes \boldsymbol{C} \cdot \boldsymbol{A}) \quad \text{A. 15}$$

And the first Piola-Kirchhoff stress tensor used in this DG/CZM method can be obtained through $\mathbf{P} = \mathbf{FS}$.

Data availability

The raw/processed test data required to reproduce these findings cannot be shared at this time due to both legal reasons and time limitations.

References

[1] Q. Liu, Y. Lin, Z. Zong, G. Sun, Q. Li, Lightweight design of carbon twill weave fabric composite body structure for electric vehicle. Compos Struct 2013;97:231-8.

[2] C.K. Park, C.D. Kan, W.T. Hollowell, Evaluation of crashworthiness of a carbon fiber reinforced polymer (CFRP) ladder frame in a body-on-frame vehicle. Int J Crashworthiness 2014;19(1):27-41.

[3] P. Feraboli, A. Masini, Development of carbon/epoxy structural components for a high performance vehicle. Compos B Eng 2004;35(4):323-30.

[4] J. Fang, G. Sun, N. Qiu, N.H. Kim, Q. Li, On design optimization for structural crashworthiness and its state of the art. Struct Multidiscip Optimiz 2017;55(3):1-29.

[5] G. Sun, T. Pang, J. Fang, G. Li, Q. Li, Parameterization of criss-cross configurations for multiobjective crashworthiness optimization. Int J Mech Sci 2017;124-125:145-57.

[6] G.L. Farely, Energy absorption in compsite materials. Journal of Composite Materials 17 (1983) 167.

[7] S. Palanivelu, W. Van Paepegem, J. Degrieck, D. Kakogiannis, J. Van Ackeren, D. Van Hemelrijck, J. Wastiels, J. Vantomme, Comparative study of the quasi-static energy absorption of small-scale composite tubes with different geometrical shapes for use in sacrificial cladding structures. Polymer Testing 29 (3) (2010) 381–396.

[8] H. Hamada, S. Ramakrishna, H. Satoh, Crushing mechanism of carbon fibre/PEEK composite tubes. Composites 26 (11) (1995) 749-755.

[9] P.H. Thronton, Energy absorption in composite structures. Journal of Composite Materials 13 (247) (1979).

[10] S.T. Pinho, P.P. Camanho and M. F. de Moura, Numerical simulation of the crushing process of composite materials. International Journal of Crashworthiness, 2004. 9(3): p. 263 - 276.

[11] V.S. Sokolinsky, K.C. Indermuehle, J.A. Hurtado. Numerical simulation of the crushing process of a corrugated composite plate. Compos A Appl Sci Manuf 2011;42(9):1119-26.

[12] X. Xiao, M.E. Botkin, N.L. Johnson. Axial crush simulation of braided carbon tubes using MAT58 in LS-DYNA. Thin-Walled Struct 2009;47(6):740-9.

[13] V.K. Goyal, N.R. Jaunky, E.R. Johnson, D.R. Ambur. Intralaminar and interlaminar progressive failure analyses of composite panels with circular cutouts. Compos Struct 2004;64(1):91–105.

[14] P. Ladeveze, A damage computational approach for composites: basic aspects and micromechanical relations. Comput Mech 1995;17(1-2):142–50.

[15] G. Vigueras, F. Sket, C. Samaniego, L. Wu, L. Noels, D. Tjahjanto, E. Casoni, G. Houzeaux, A. Makradi, J. M. Molina-Aldareguia, M. Vázquez, A. Jérusalem, An XFEM/CZM implementation for massively parallel simulations of composites fracture. Composite Structures 125 (2015) 542–557.

[16] S. Palanivelu, Energy Absorption of Crushable Tubes for Protective Structures under Static, Impact and Blast Loading. PhD Dissertation, Ghent University, 2011.

[17] B. Green, M. Wisnom, S. Hallett, An experimental investigation into the tensile strength scaling of notched composites. Compos Part A: Appl Sci Manuf 2007;38(3):867–78.

[18] S.R. Hallett, WG. Jiang, B. Khan, M.R. Wisnom. Modelling the interaction between matrix cracks and delamination damage in scaled quasi-isotropic specimens. Compos Sci Technol 2008;68(1):80–9.

[19] XP. Xu, A. Needleman, Numerical simulations of fast crack growth in brittle solids, Journal of the Mechanics and Physics of Solids 42 (9) (1994) 1397 - 1434, ISSN 0022-5096, doi:10.1016/0022-5096(94)90003-5.

[20] S.H. Song, G.H. Paulino, W.G. Buttlar. A bilinear cohesive zone model tailored for fracture of asphalt concrete considering viscoelastic bulk material. Eng Fract Mech 2006;73(18):2829–48.

[21] N. Blal, L. Daridon, Y. Monerie, S. Pagano, Criteria on the artificial compliance inherent to the intrinsic cohesive zone. Comptes Rendus Mécanique 2011;339(12):789–95.

[22] P. Zavattieri, H. Espinosa, Grain level analysis of crack initiation and propagation in brittle materials. Acta Materialia 2001;49(20):4291–311.

[23] G.T. Camacho, M. Ortiz, Computational modelling of impact damage in brittle materials, International Journal of Solids and Structures 33 (20-22) (1996) 2899-2938, ISSN 0020-7683.

[24] A. Pandol, P. Guduru, M. Ortiz, A. Rosakis, Three dimensional cohesive-element analysis and experiments of dynamic fracture in C300 steel, International Journal of Solids and Structures 37 (27) (2000) 3733-3760, ISSN 0020-7683, doi:10.1016/S0020-7683(99)00155-9.

[25] M. Lee, E.Y. Kim, Y.H. Yoo, Simulation of high speed impact into ceramic composite systems using cohesive-law fracture model[J]. International Journal of Impact Engineering. 2008, 35(12): 1636-1641.

[26] X. Zhang, T. Liu, X. Qiu, Orthotropic node-separation finite element method for composite laminate in hypervelocity impact simulation[J]. Acta Astronautica. 2017, 140(2017): 78-90.

[27] N. Moës, T. Belytschko, Extended finite element method for cohesive crack growth. Eng Fracture Mech 2002;69(7):813–33.

[28] J. Dolbow, N. Moës, T. Belytschko, An extended finite element method for modeling crack growth with frictional contact. Comput Methods Appl Mech Eng 2001;190(51-52):6825–46.

[29] J. Mergheim, E. Kuhl, P. Steinmann, A hybrid discontinuous Galerkin/interface method for the computational modelling of failure, Communications in Numerical Methods in Engineering 20 (7) (2004) 511-519.

[30] R. Radovitzky, A. Seagraves, M. Tupek, L. Noels, A scalable 3D fracture and fragmentation algorithm based on a hybrid, discontinuous Galerkin, cohesive element method, Computer Methods in Applied Mechanics and Engineering 200 (2011) 326-344, ISSN 0045-7825, doi:10.1016/j.cma.2010.08.014.

[31] L. Wu, D. Tjahjanto, G. Becker, A. Makradi, A. Jerusalem, L. Noels, A micro-meso-model of intra-laminar fracture in fiber-reinforced composites based on a discontinuous Galerkin/cohesive zone method, Engineering Fracture Mechanics 104 (2013) 162-183, ISSN 0013-7944.

[32] G. Becker, C. Geuzaine, L. Noels, A one Field Full Discontinuous Galerkin Method for Kirchhoff-Love Shells Applied to Fracture Mechanics, Computer Methods in Applied Mechanics and Engineering 200 (2011) 3223-3241, ISSN 0045-7825,
doi:10.1016/j.cma.2011.07.008.

[33] G. Becker, L. Noels, A full discontinuous Galerkin formulation of non-linear Kirchhoff-Love shells: elasto-plastic finite deformations, parallel computation & fracture applications, International Journal for Numerical Methods in Engineering 93 (2013) 80{117, ISSN 1097-0207, doi:10.1002/nme.4381.

[34] L. Noels, R. Radovitzky, A general discontinuous Galerkin method for finite hyperelasticity. Formulation and numerical applications, Int. J. Numer. Methods Engrg. 68 (1) (2006) 64–97.

[35] L. Noels, R. Radovitzky, An explicit discontinuous Galerkin method for nonlinear solid dynamics. Formulation, parallel implementation and scalability properties, Int. J. Numer. Methods Engrg. 74 (2007) 1393–1420.

[36] CM3 Group in University of Liege: http://www.ltas-cm3.ulg.ac.be/staff.htm

[37] P.P. Camanho and S.R. Hallett, Numerical Modelling of Failure in Advanced Composite Materials, Part One Chapter 2, 2015.

[38] A. Turon, P. Camanho, J. Costa, C. Davila, A damage model for the simulation of delamination in advanced composites under variable-mode loading, Mechanics of Materials 38 (11) (2006) 1072-1089, ISSN 0167-6636, doi: 10.1016/j.mechmat.2005.10.003.

[39] A. Turon, C. D~avila, P. Camanho, J. Costa, An engineering solution for mesh size effects in the simulation of delamination using cohesive zone models, Engineering Fracture Mechanics 74 (10) (2007) 1665-1682, ISSN 0013-7944, doi: 10.1016/j.engfracmech.2006.08.025.

[40] CG. Davila, PP. Camanho, MF. de Moura. Mixed-mode decohesion elements for analyses of progressive delamination In: 42nd AIAA/ASME/ASCE/AHS/ASC structures, structural dynamics, and materials conference and exhibit, Seattle 2001.

[41] L. Wu, F. Sket, J.M. Molina-Aldareguia, A. Makradi, L. Adam, I. Doghri, L. Noels, A study of composite laminates failure using an anisotropic gradient-enhanced damage mean-field homogenization model, Composite Structures 126 (2015) 246-264.

[42] S.T. Pinho, L. Iannucci, P. Robinson, Formulation and implementation of decohesion elements in an explicit finite element code, Composites: Part A 37 (2006) 778–789.

[43] S.S. Mulay, G. Becker, R. Vayrette, J.-P. Raskin, T. Pardoen, M. Galceran, S. Godet, L. Noels, Multiscale modelling framework for the fracture of thin brittle polycrystalline films: application to polysilicon. Comput Mech (2015) 55:73–91.

[44] S. Palanivelu, W. Van Paepegem, J. Degrieck, J. Van Ackeren, D. Kakogiannis, D. Van Hemelrijck, J. Wastiels, J. Vantomme, Experimental study on the axial crushing behaviour of pultruded composite tubes. Polymer Testing 29 (2) (2010) 224–234.

[45] H. Hamada and S. Ramakrishna, Scaling effects in the energy absorption of carbon-fiber/PEEK composite tubes. Composites Science and Technology, 1995. 55(3): p. 211-221.

[46] Pyrofil Department. Mechanical Properties of PYROFIL TR 360E250S Unidirectional Composite. Technical report, Mitsubishi Rayon Co., Ltd., Carbon Fiber and Composite Materials Division, December 2013.

[47] S. Fonteyn, L. Pyl, D. Van Hemelrijck, Fracture toughness of composite materials under Mode I delamination assisted by Digital Image Correlation, 17th International Conference on Experimental Mechanics (Abstract), Rhodes, Greece, July 2016.

[48] R.D.B. Sevenois, D. Garoz, E. Verboven, S.W.F. Spronk, F.A. Gilabert, M. Kersemans, L. Pyl, W. Van Paepegem, Multiscale approach for identification of transverse isotropic carbon fibre

properties and prediction of woven elastic properties using ultrasonic identification, Composites Science and Technology 168 (2018) 160-169.
[49] A. Arteiro, G. Catalanotti, A.R. Melro, P. Linde, & P.P. Camanho, Micro-mechanical analysis of the in situ effect in polymer composite laminates. Composite Structures (2014), 116, 827-840.
[50] Pyrofil Department. Mechanical Properties of PYROFIL TR 50S15L Carbon Fiber. Technical report, Mitsubishi Rayon Co., Ltd., Carbon Fiber and Composite Materials Division, June 2013.
[51] M.J. Laffan, S.T. Pinho, P. Robinson, L. Iannucci, Measurement of the in situ ply fracture toughness associated with mode I fibre tensile failure in FRP. Part I: data reduction, Composites Science and Technology 70 (2010) 606–613.
[52] M.J. Laffan, S.T. Pinho, P. Robinson, A.J. McMillan, Translaminar fracture toughness testing of composites: A review, Polymer Testing 31 (2012) 481–489.
[53] K. Honjo, Fracture toughness of PAN-based carbon fibres estimated from strength-mirror size relation, Carbon 41 (2003) 979–984.
[54] GMSH version 4.4.1: http://gmsh.info/.
[55] L. Wu, G. Becker, l. Noels, Elastic damage to crack transition in a coupled nonlocal implicit discontinuous Galerkin/extrinsic cohesive law framework. Comput Methods Appl Mech Eng 279 (2014) 379 – 409.
[56] S. Palanivelu, W. Van Paepegem, J. Degrieck, J. Van Ackeren, D. Kakogiannis, J. Wastiels, D. Van Hemelrijck, J. Vantomme, Parametric study of crushing parameters and failure patterns of pultruded composite tubes using cohesive elements and seam: Part II – Multiple delaminations and initial geometric imperfections, Polymer Testing 29 (2010) 803–814.
[57] G. Zhu, G. Sun, G. Li, A. Cheng, Q. Li, Modeling for CFRP structures subjected to quasi-static crushing, Composite Structures 184 (2018) 41–55.
[58] J. Bonet, A.J. Burton, A simple orthotropic, transversely isotropic hyperelastic constitutive equation for large strain computations. Comput Methods Appl Mech Engng 1998, 162(1-4):151–64.